Modelling of impingement phenomena for molten metallic droplets with low to high velocities

H. Tabbara [a], S. Gu [a,b,*]

[a] School of Engineering Science, University of Southampton, Highfield, Southampton SO17 1BJ, United Kingdom
[b] Xi'an Jiaotong-Liverpool University, No.111 Ren'ai Road, Suzhou Dushu Lake Higher Education Town, Suzhou 215123, China

A R T I C L E   I N F O

A B S T R A C T

Thermal spray coatings are formed by accelerating a stream of powder particles towards a targeted substrate surface where they impact, deform, and adhere. A fundamental understanding of the splat formation can pave the way for future developments in thermal spray technology through better understanding. Numerical modelling is applied in this investigation which simulates the detailed transient flow of a molten metal droplet impacting, deforming, and solidifying on a flat, solid substrate. The computations are carried out on a fixed Eularian structured mesh using a volume of fluid method to simulate the boundary between the metallic and atmospheric-gas phases. The results shed light on the break-up phenomena on impact and describe in detail how the solidification process varies with an increasing impact velocity.

1. Introduction

Thermal spray coatings are formed by accelerating a stream of molten, semi molten or solid powder particles towards a targeted substrate surface. The particles initially impact onto the substrate where they are required to deform and adhere to the surface. These particles then impinge onto one another, building up the coating particle by particle in a lamellar structure. The degree of deformation of these particles and their adhesion strength to the substrate can be attributed to several factors, including: particle impact velocity, particle size, particle phase content, particle material properties, wetting of the substrate, temperature of the substrate and substrate roughness. While experimental investigations can link these factors to a final coating morphology, powerful computer aided simulations are now providing further scientific insight to the deposition process and the physics of the coating build up.

Measuring and understanding the particle-laden flow is not only restricted by the casing of the thermal spray gun, but also made difficult by the high velocities and temperatures at which the systems often operate. Therefore much effort has been invested in the modelling and simulation of the particle-laden jets. A recent review of these modelling efforts can be found [1]. The results obtained have greatly enhanced scientific understanding within the thermal spray coating community. By coupling the gas and particulate phases these models are capable of simulating the transient velocity, temperature, and phase content of the powders travelling through a thermal spray device. Prior to impingement an individual particle can be predicted and input into a focused impingement model in order to recreate a coating structure.

The second stage of the modelling process involves the simulation of particle impingement. To date, the simulations of fully molten droplet impingements have improved the understanding of particle deformation and adhesion in thermal spraying, which are well reviewed by Chandra and Fauchais [2] and Kamnis and Gu [3]. At present the latest models are capable of describing several physical phenomena which arise during the process of molten droplet impingement and their modelling strategies are outlined as follows.

Computational fluid dynamics (CFD) based volume of fluid method (VOF) is utilized in almost all cases to track the deforming surface of the molten droplet [3–6]. The fluid surface tension force at the boundary between the droplet and the surrounding gas is included as a body force in the momentum conservation equation [3,6]. The solidification process has been equated using different methods. The decrease in velocity due to solidification may be mathematically described by introducing a sink term within the momentum conservation equation [3]. In this method the average viscosity and density of the material occupying a computational cell **are** calculated based on the volume fraction of liquid and solid and their associated densities. Alternatively, a fixed velocity method is adopted by Pasandideh-Fard et al. [7], whereby the velocity

* Corresponding author at: Xi'an Jiaotong-Liverpool University, No.111 Ren'ai Road, Suzhou Dushu Lake Higher Education Town, Suzhou 215123, China.
  E-mail addresses: s.gu@soton.ac.uk, sai.gu@xjtlu.edu.cn (S. Gu).

Nomenclature and units

General symbols

C_p	Specific heat capacity at constant pressure
D_0	initial particle diameter
g	gravitational acceleration
h_c	convective heat transfer coefficient between the droplet and atmosphere
h	sensible heat
H	total heat
ΔH	latent heat content
k	thermal conductivity
L	latent heat when in liquid phase
t	time
T	temperature
V_0	initial particle velocity
v	velocity

Greek symbols

α	thermal diffusivity
β	liquid fraction
μ	viscosity

σ	surface tension
ρ	density

Dimensionless numbers

Biot number $Bi = \frac{h_c D_0}{k_d}$
Nusselt number $Nu = \frac{h_c D_0}{k_g} = 2 + 0.6 Re^{1/2} Pr^{1/3}$
Peclet number $Pe = \frac{t_c}{t_s} = \frac{D_0 V_0}{\alpha}$
Prandtl number $Pr = \frac{C_p \mu_g}{k_g}$
Reynolds number $Re_g = \frac{\rho_g V_0 D_0}{\mu_g}$ or $Re_d = \frac{\rho_d V_0 D_0}{\mu_d}$
Time $t^* = \frac{V_0 t}{D_0}$
Weber number $We = \frac{\rho_d V_0^2 D_0}{\sigma}$

Subscript symbols

d	droplet
g	atmospheric gas
p	primary phase
q	one of several phases
w	wall
∞	bulk region

---

vector within the momentum conservation equation is directly multiplied by the liquid phase fraction within the associated computational cell. Hence, if the cell is fully solid then the contents of the cell are stationary. During both of these solidification methods an enthalpy formulation takes into account the combined sensible enthalpy and the latent heat of solidification, which completes the energy equation and allows prediction of the temperature profile through the impinging droplet. The investigations found in [3,5,7] couple the heat energy transfer between the droplet and the substrate which plays a vital role in simulating the splat morphology by controlling the rate of cooling and solidification. The more advanced computational models include a thermal contact resistance [3,7], which is physically created by air enclosed within the roughness of the substrate and acts as a resistance to the coupled heat transfer process.

Validation of these models has highlighted their ability to successfully predict the rate of spreading and solidification of a single molten droplet impingement [3,7] with the correct number of fingers surrounding a three dimensional splat [8]. Recent image based validations have been targeted towards simulating more than one droplet and with the inclusion of uneven substrate surfaces, which also compare extremely well alongside photographic imaging [9–11].

This study builds upon previous work by Kamnis [3,8] by closely examining the impingement process during impact and solidification. The work sheds light on the interaction between the molten metal droplet and the ambient air during its initial stages of impact. Additionally, the work demonstrates for the first time that modelling using the CFD methods can produce high levels of detail at the particle/substrate interface, which can be utilised in the future to explain mechanical bonding structures. The impact velocity in this investigation is increased to bridge the gap between the previous low velocity simulations and the realistic velocities found during thermal spraying.

2. Summary of numerical methods

A 2.2 mm molten tin (Sn) particle at an initial uniform temperature of 519 K is simulated to impact onto a flat, stainless steel substrate at a temperature of 298 K. The simulated droplet impact velocities are: 4 ms^{-1}, 10 ms^{-1}, 100 ms^{-1} and 400 ms^{-1}. The Biot number (Bi) of the spherical droplet can be estimated by calculat-

ing the convective heat transfer coefficient at the surface of the droplet using the Ranz and Marshall correlation [12] as outlined in Eq. (1). The values of the Bi number for the molten droplet travelling through air at atmospheric condition are given in Table 1, along with the constituent values of Nu, Re and Pr. The Bi numbers for all scenarios are well below unity and therefore indicate that a uniform temperature distribution through the droplet is a realistic assumption.

$$Nu = 2 + 0.6 Re_g^{\frac{1}{2}} Pr^{\frac{1}{3}} \tag{1}$$

The dimensions for the axisymmetric domain are provided in Fig. 1, including the initial particle–substrate separation distance. The 2D axisymmetric domain consists of 240,000 structured computational cells and a refined grid is utilized at the substrate surface. The numerical methodology is based on previous work and a description can be found in [3]. A summary of the flow and thermal modelling approach is outlined in Table 1.

2.1. Flow model

The VOF model is used to track the droplet and air as two immiscible fluids by solving a single set of momentum equations. This method is carried out by tracking the volume fraction of each of the fluids throughout the computational domain. The compressive interface capturing scheme (CICSAM) by Ubbink and Issa [13] is applied as the discretization scheme due to its suitability for flows with high viscosity ratios between the immiscible phases. The full mathematical description of the CICSAM scheme can be found in [13].

The tracking of the interface between the gas phase and molten droplet phase is based on the volume fraction continuity equation,

Table 1
Values of Nu, Re, Pr and Bi for a 2.2 mm molten tin droplet at a temperature of 519 K travelling through air under standard atmospheric condition.

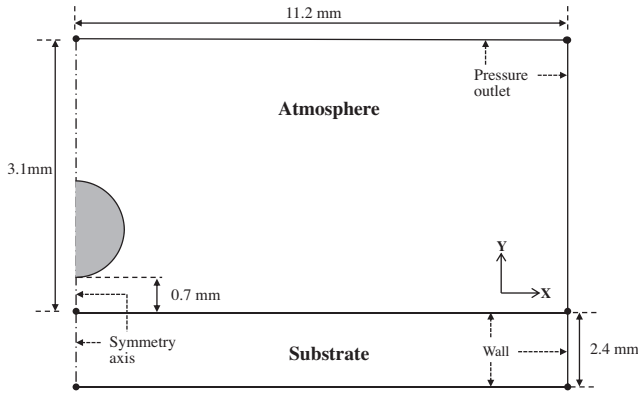|	4 ms^{-1}	10 ms^{-1}	100 ms^{-1}	400 ms^{-1}
Nu	15.345	23.101	68.727	135.454
Re$_g$	602.000	1506.091	15060.914	60243.657
Pr	0.744	0.744	0.744	0.744
Bi	0.011	0.017	0.050	0.098

Fig. 1. Schematic diagram of the axisymmetric computational domain for the impingement of a 2.2 mm molten tin droplet.

as given by Eq. (2). Where v is the velocity, ρ is the density, α is the volume fraction and t is the time. The subscript q implies one of the phases. For the surrounding air, which is treated as the primary phase, the volume fraction is computed using the constraint shown in Eq. (3), where n is the number of phases and is equal to 2. The density ρ and viscosity μ within each computational cell are calculated based on the volume fraction of each phase, as in Eqs. (4) and (5), where the subscripts 1 and 2 represent the primary and secondary phases, respectively.

$$\frac{1}{\rho_q}\left[\frac{\partial}{\partial t}(\alpha_q \rho_q) + \nabla \cdot (\alpha_q \rho_q \vec{v}_q)\right] = 0 \quad (2)$$

$$\Sigma_{i=1}^{n} \alpha_i = 1 \quad (3)$$

$$\rho = \alpha_2 \rho_2 + (1 - \alpha_2)\rho_1 \quad (4)$$

$$\mu = \alpha_2 \mu_2 + (1 - \alpha_2)\mu_1 \quad (5)$$

The volume-fraction-averaged material properties are then applied in the momentum and energy conservation equations are given in Eqs. (6) and (7) where g is the gravitational acceleration, H is the total heat, k is the thermal conductivity, p is the pressure, and T is the temperature. The resulting velocity and energy fields are therefore shared between the two phases.

$$\frac{\partial}{\partial t}(\rho \vec{v}) + \nabla \cdot (\rho \vec{v}\,\vec{v}) = -\nabla p + \nabla \cdot [\mu(\nabla \vec{v} + \nabla \vec{v}^T)] + \rho \vec{g} + F_{vol} + S_y \quad (6)$$

$$\frac{\partial}{\partial t}(\rho H) + \nabla \cdot (\rho \vec{v} H) = \nabla \cdot (k\nabla T) \quad (7)$$

The continuum surface tension force, F_{vol}, is calculated by the method of Brackbill et al. [14] using the fluid densities at the interface and the droplet surface tension. Its value appears on the right-hand-side of the momentum equation as a source term. The methods of Brackbill et al. are also utilized to predict the curvature of the droplet surface close to the wall using the computed tangential and normal flow velocity components along the wall, and the contact angle of the droplet at the substrate surface [14]. The contact angles are obtained from the measured results of Aziz and Chandra [15]. In this instance an initial angle of 70° is introduced and the dimensionless transition time (as defined in the table of dimensionless numbers in the appendix) from 70° to 140° is calculated to be 0.07. A porosity function is applied, known as the Darcy Law, which acts as a sink term (S_y) within the momentum equation. The solidifying liquid incurs a decrease in momentum until the droplet becomes stationary due to complete solidification.
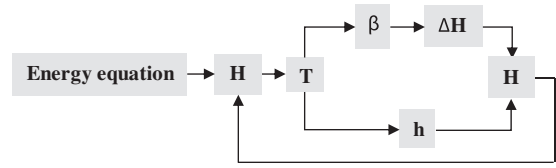

Fig. 2. Iterative enthalpy formulation during phase transition, including the latent heat of solidification.

2.2. Thermal model

The particle is initialized with a uniform temperature of 519 K. An enthalpy balance is used in order to calculate the liquid fraction of solid and liquid within a computational cell during the solidification of the droplet. The total enthalpy of the material, H, is calculated as the sum of the sensible enthalpy, h, and latent heat, ΔH, as given in Eq. (8). A computational cell may reach a temperature which lies between the solidus and liquidus temperatures. Within this region the material is said to be within its mushy state, consisting of both solid and liquid phases. The liquid fraction within the mushy region is termed β and L is the latent heat when in liquid phase.

$$H = h + \Delta H \quad (8)$$

where,

$$h = h_{ref} + \int_{T_{ref}}^{T} C_p dT \quad (9)$$

$$\Delta H = \beta L \quad (10)$$

As the temperature increases or decreases during the transition between liquid and solid, the latent heat is either absorbed or dissipated respectively. This change in temperature determines the fractional change in liquid concentration Eq. (8). The calculation of temperature is therefore achieved by a sub-iteration to match the total enthalpy from the energy equation (Eq. (7)) with the combined values of sensible enthalpy and latent heat (Eq. (8)) as outlined in Fig. 2.

$$\begin{aligned}
\beta &= 0 \quad \text{if } T < T_{solidus} \\
\beta &= 1 \quad \text{if } T > T_{liquidus} \\
\beta &= \frac{T - T_{solidus}}{T_{liquidus} - T_{solidus}} \quad \text{if } T_{solidus} < T < T_{liquidus}
\end{aligned} \quad (11)$$

The heat transfer process through the substrate is by conduction. In reality air is entrapped within the roughness of the material surface which acts as thermal resistance. The model takes into account the air entrapment by applying a thermal resistance to the flow of heat energy to the substrate. A value of $1.8 \times 10^{-6}\,\mathrm{m^2 K\,W^{-1}}$ for

Table 2
Material properties.

Impinging droplet	Tin (Sn)
Substrate material	Stainless steel (SS)
Droplet initial temperature	519 K
Substrate initial temperature	298 K
Solidus temperature (Sn)	504 K
Liquidus temperature (Sn)	506 K
Thermal conductivity (liquid Sn)	33.6 W (m K)$^{-1}$
Thermal conductivity (solid Sn)	62.2 W (m K)$^{-1}$
Thermal conductivity (SS)	14.9 W (m K)$^{-1}$
Density (liquid Sn)	6980 kg (m)$^{-3}$
Density (solid Sn)	7200 kg (m)$^{-3}$
Density (SS)	7900 kg (m)$^{-3}$
Droplet surface tension	0.566 N (m)$^{-1}$
Specific heat capacity (Sn)	244 J (kg K)$^{-1}$
Specific heat capacity (SS)	477 J (kg K)$^{-1}$
Latent heat of solidification	58500 J (kg)$^{-1}$

the thermal contact resistance is applied which corresponds to a stainless steel substrate roughness of 0.06 μm [16]. The droplet and substrate material properties are summarized in Table 2.

3. Results and discussion

3.1. Experimental comparisons and background

The variation in spread factor (D/D_0) with time of the simulated particle is plotted alongside experimental measurements in Fig. 3. The experimental results are of the same scenario, whereby a 2.2 mm Sn droplet at 519 K impacts at a velocity of 4 ms^{-1} on a substrate of 0.06 μm roughness [16]. The results show a good level of concordance during all stages of spreading, retardation, and re-coil. The final splat diameter of the modelled droplet and the experimental image are also physically similar as compared in Fig. 4, with a thin, uneven central surface and thick, solidified rim around the outside edge.

The transient motion of the simulated droplet impacting at 4 ms^{-1} is depicted in Fig. 5 showing a good likeness to previous numerical simulations [3,9]. The particle impinges onto the surface, where it deforms and begins to spread outwards. The molten material then begins to slow and cool due to heat transfer to the substrate. Solidification and retardation at the periphery of the splat creates matter to be ejected, as shown in Fig. 5. Several exper-
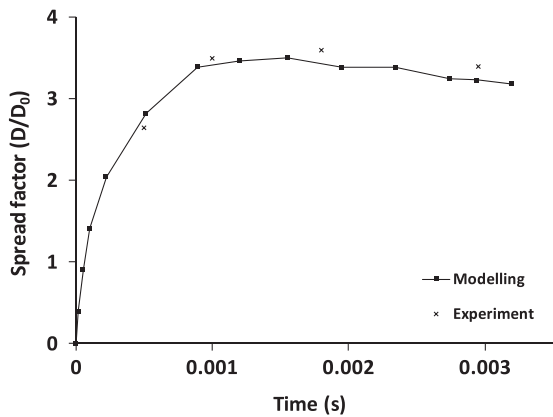
imental and numerical studies have commented on this process of matter ejection [2,3,17–19], and a detailed numerical study characterizes the process in detail [20].

3.2. Spreading

Fig. 6 plots the variation of spread factor with dimensionless time, t^*, for the simulated 2.2 mm droplet impinging at 4, 10, 100 and 400 ms^{-1}. The values of droplet Weber number (We) and droplet Reynolds number (Re_d) are listed in Table 3, and greatly exceed unity in all cases. This information indicates that both the surface tension and viscous forces play a negligible role in controlling the

Fig. 5. Development of the splat formation with an impingement velocity of 4 ms^{-1}.

Fig. 3. Comparison of simulated and experimentally measured [16] spread factors for a molten tin droplet impinging at 4 ms^{-1} and initial temperature of 519 K onto a stainless steel substrate at an initial temperature of 298 K.
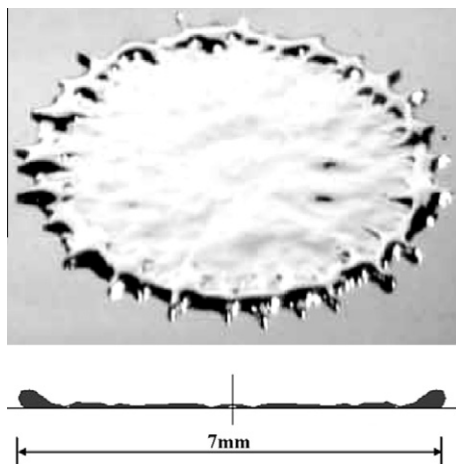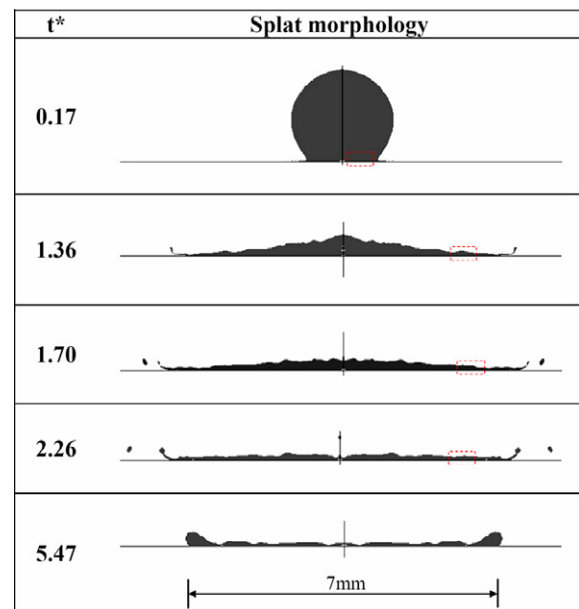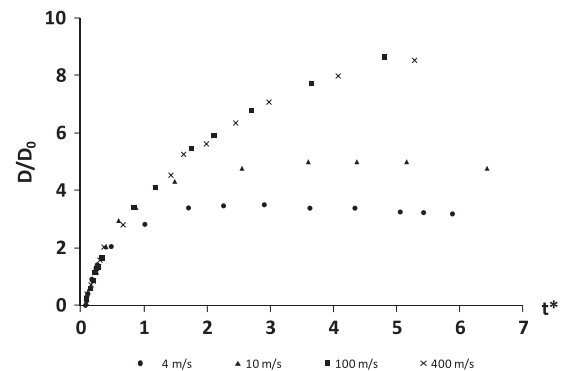

Fig. 4. Physical comparison between simulated and experimental splat shape for an impact velocity of 4 ms^{-1} [16].

Fig. 6. Comparison of droplet spread factors with increasing impact velocity.

Table 3
Dimensionless numbers for a 2.2 mm molten tin droplet at a temperature of 519 K travelling through air at standard temperature and pressure.

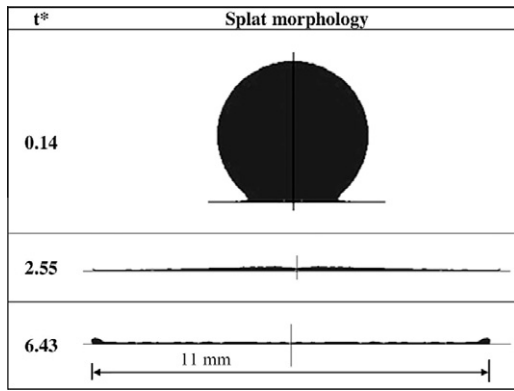| Dimensionless parameter	4 ms^{-1}	10 ms^{-1}	100 ms^{-1}	400 ms^{-1}
Re_d	27,920	69,800	698,000	2,792,000
We	434.0	2713	271,307	4,340,918
Pe	1.892	4.73	47.3	189.2

Fig. 7. Splat formation with an impingement velocity of 10 ms^{-1}.

motion of the droplet at the time of impact compared to the inertial forces.

When impacting at 4 ms^{-1} the droplet reaches its maximum splat diameter after roughly 0.002 s. The surface tension forces further draw the particle edges inwards and the particle is arrested at roughly 0.003 s. The modelled final spat formation of a droplet impacting at 10 ms^{-1} is given in Fig. 7, revealing a thinner, more even internal surface and smaller sized rim when compared to the 4 ms^{-1} droplet.

The solidification and spreading kinetics are linked by the droplet Peclet number (Pe). If Pe greatly exceeds unity then one can assume the spreading rate is far greater than the heat conduction and solidification, and therefore solidification bears a negligible effect on the final splat shape. This is demonstrated by the simulation of the Sn droplet impacting at 100 ms^{-1} and 400 ms^{-1}. For these higher velocity impingements, Pe is equal to 47 and 189, respectively, and the splat spreads to the outside edge of the computational domain in a short space of time. During this period, solidification has made little affect on the spreading kinetics and is controlled by the droplet momentum. For this reason the spread factor variation against dimensionless time is simulated to be almost identical for an impacting droplet at 100 ms^{-1} and 400 ms^{-1}, as depicted in Fig. 6, implying that during this period both droplets exhibit the same overall impact characteristics, but at a different rates.

3.3. Impact phenomena

This section investigates the impacting droplet flow and break-up phenomena around the initial impact zone during the early stages of impingement. The simulations indicate that the droplet break-up around the initial impact zone at an impact velocity of up to 10 ms^{-1} is negligible. However, when the velocity is increased to 100 ms^{-1} the Rayleigh–Taylor instabilities form at the droplet–air interface due to the increased air resistance against the flow of the droplet, producing an uneven surface boundary. As the magnitude of these perturbations grows the molten liquid, by virtue of its surface tension, minimizes its surface by creating small fragmented droplets, as exhibited in Fig. 8a and b. The vorticies at the edge of the impinging droplet further destabilize the surface and are strengthened with higher impact velocities.

At high impact velocities of 100 ms^{-1} and 400 ms^{-1} the air is entrapped within the particle through the underside of the droplet on impact and by penetration of the vortex at the outside surface, as shown in Fig. 8. The entrapped gas is then forced outwards due to the spreading of the droplet and higher pressure at the centre of the impact zone. Together the Rayleigh–Taylor instabilities and the air entrapment cause shedding of small particles on impact.
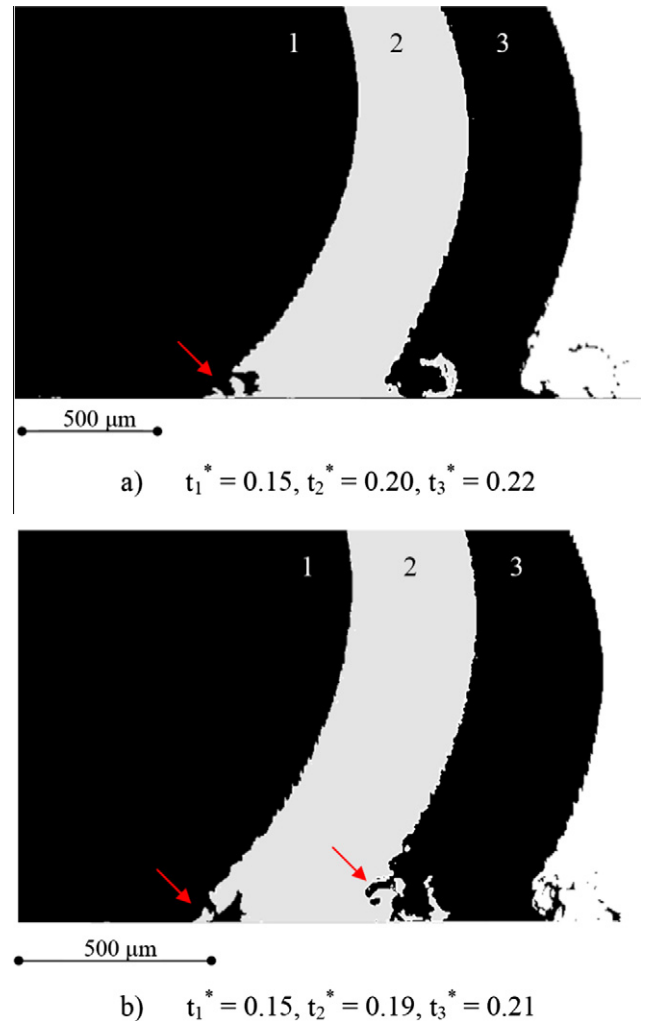

a) $t_1{}^* = 0.15$, $t_2{}^* = 0.20$, $t_3{}^* = 0.22$

b) $t_1{}^* = 0.15$, $t_2{}^* = 0.19$, $t_3{}^* = 0.21$

Fig. 8. The process of droplet break-up on impact at (a) 100 ms^{-1} and (b) 400 ms^{-1} with air entrapments highlighted.
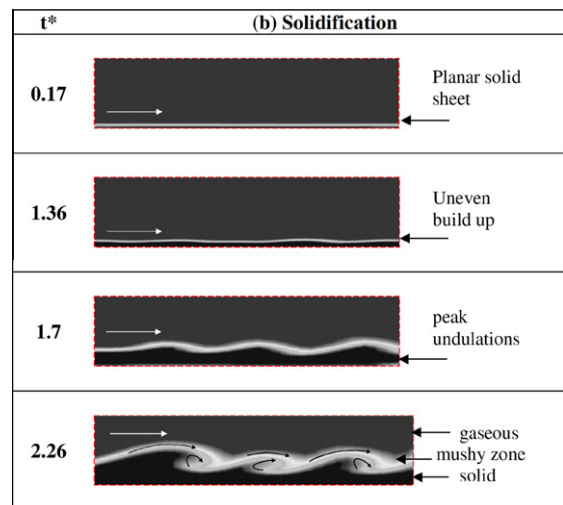

Fig. 9. The solidification process with an impingement velocity of 4 ms^{-1}. Sections taken from highlighted zones in Fig. 5.

Fig. 8 also highlights how by increasing the velocity from 100 to 400 ms^{-1} the molten droplet is woven inwards creating larger pores.

3.4. Solidification process

The transient impact morphology of the 2.2 mm Sn particle impacting at 4 ms^{-1} is exhibited in Fig. 5, and the process of solidification within the highlighted zones are depicted in Fig. 9. At $t^* = 0.17$ (9.42×10^{-5} s) planar solidification begins, producing a smooth level sheet of solidified Sn at the substrate surface. At $t^* = 1.36$ (7.47×10^{-4} s) the solidified Sn begins to build up unevenly and by $t^* = 1.7$ (9.36×10^{-4} s) the peaks of solidified Sn reach their maximum amplitude of roughly 15 μm. A wave like process is then initiated whereby the liquid material is woven inwards as it solidifies, as depicted in Fig. 9. The molten fluid vorticities produced are known as Kelvin–Helmholtz instabilities and occur due to velocity shearing. This folding phenomenon was hypothesised to occur at the substrate surface of thermal spray coatings by Grujicic et al. [21] and has been recently observed in thermal spraying when carrying out TEM scans of a final coating cross section [22]. The TEM scans in [22] show that the particles melt the substrate surface on impact and mechanical interlocking (mechanical keying) occurs. This mechanical interlocking has been documented to chiefly determine the adhesion strength of a coating to the substrate in thermal spray coatings [23].

In this case, for the impinging 10 ms^{-1} particle the size of the undulating peaks are found to be too shallow to produce wave mixing because of its higher Pe. As a result the molten droplet does not solidify rapidly enough to create solid peaks with amplitude great enough to induce wave-like mixing. The results of this case indicate that beyond 100 ms^{-1} the rate of spreading occurs so rapidly that conduction of heat becomes negligible. As a result at an impact of 100 ms^{-1} and 400 ms^{-1} little or no solidification is observed and the splat film spreads to the edge of the computational domain.

4. Conclusion

The simulation results for a 2.2 mm tin droplet at 519 K and impact velocity of 4, 10, 100 and 400 ms^{-1}. The simulated splat formation of a droplet impacting at 10 ms^{-1} reveals a thinner, more even internal surface and smaller sized rim when compared to the 4 ms^{-1} droplet. For the higher velocity impingements the splat spreads to the outside edge of the computational domain in a short space of time and the extent of solidification is negligible.

The simulations indicate that for a 2.2 mm Sn droplet at 519 K little or no fragmentation will occur around the initial impact zone at impact velocities of up to 10 ms^{-1}. When the impact velocity is increased to 100 ms^{-1} fine fragmented droplets are produced. With an impact velocity of 400 ms^{-1} the droplet is woven inwards creating large pores.

The solidification process may consist of up to three stages: planar solidification; uneven solidification and wave mixing. The detailed development of the solidifying splat morphology presented in this study highlights the potential of this computational method to be capable of modelling mechanical interlocking structures. Future modelling work can now focus on the detailed interaction of more than one micron sized droplet and a melted substrate surface so that a deeper understanding of the mechanical bonding structure at the substrate can be established.

References

[1] B.M. Cetegen, S. Basu, Review of modeling of liquid precursor droplets and particles injected into plasmas and high-velocity oxy-fuel (HVOF) flame jets for thermal spray deposition applications, J. Therm. Spray Tech. 18 (2009) 769.
[2] S. Chandra, P. Fauchais, Formation of solid splats during thermal spray deposition, J. Therm. Spray Tech. 18 (2009) 148.
[3] S. Kamnis, S. Gu, Numerical modelling of droplet impingement, J. Phys. D 38 (2005) 3664.
[4] M.R. Ivosevic, A. Cairncross, R. Knight, 3D prediction of thermally sprayed polymer splats: modelling particle acceleration, heating and deformation on impact with a flat substrate, Int. J. Heat Mass Transfer 49 (2006) 3285.
[5] A.M. Ahmed, R.H. Rangel, Metal droplet deposition on non-flat surfaces; effects of substrate morphology, Int. J. Heat Mass Transfer 45 (2002) 1077.
[6] M. Bussmann, J. Mostaghimi, S. Chandra, On a three-dimensional volume tracking model of droplet impact, Phys. Fluids 11 (1999) 1406.
[7] M. Pasandideh-Fard, R. Bhola, S. Chandra, J. Mostaghimi, Deposition of tin droplets on a steel plate: simulations and experiments, Int. J. Heat Mass Transfer 41 (1998) 2929.
[8] S. Kamnis, S. Gu, T.J. Lu, C. Chen, Numerical modelling of sequential droplet impingements, J. Phys. D 41 (2008) 1.
[9] R. Ghafouri-Azar, J. Mostaghimi, S. Chandra, Numerical study of impact and solidification of a droplet over a deposited frozen splat, Int. J. Comput. Fluid. D 18 (2004) 133.
[10] R. Ghafouri-Azar, Z. Yang, S. Chandra, J. Mostaghimi, Impact of molten metal droplets on the tip of a pin projecting from a flat surface, Int. J. Heat. Fluid. Fl. 26 (2005) 334.
[11] M. Pasandideh-Fard, S. Chandra, J. Mostaghimi, A three-dimensional model of droplet impact and solidification, Int. J. Heat Mass Transfer 45 (2002) 2229.
[12] W.E. Ranz, W.R. Marshall, Evaporation from drops (Part I), Chem. Eng. Prog. 48 (1952) 141.
[13] O. Ubbink, R.I. Issa, A method for capturing sharp fluid interfaces on arbitrary meshes, J. Comput. Phys. 153 (1999) 26.
[14] J.U. Brackbill, D.B. Kothe, C. Zemach, A continuum method for modeling surface tension, J. Comput. Phys. 100 (1992) 335.
[15] S.D. Aziz, S. Chandra, Impact recoil and splashing of molten metal droplets, Int. J. Heat. Mass. Transfer 43 (2000) 2841.
[16] S. Shakeri, S. Chandra, Splashing of molten tin droplets on a rough steel surface, Int. J. Heat Mass Transfer 45 (2002) 4561.
[17] J. Mostaghimi, M. Pasandideh-Fard, S. Chandra, Dynamics of splat formation in plasma spray coating process, Plasma Chem. Plasma Process 22 (2002) 59.
[18] M. Fukumoto, Y. Huang, Flattening mechanisms in thermal sprayed nickel particle impinging on a flat substrate surface, J. Therm. Spray Tech. 8 (1999) 427.
[19] M. Pasandideh-Fard, V. Pershin, S. Chandra, J. Mostaghimi, Splat shapes in a thermal spray coating process: simulations and experiments, J. Therm. Spray Tech. 11 (2002) 206.
[20] H. Tabbara, S. Gu, Numerical study of semi-molten droplet impingement, Appl. Phys. A 104 (2011) 1011–1019.
[21] M. Grujicic, J.R. Saylor, D.E. Beasley, W.S. De Rosset, D. Helfritch, Computational analysis of the interfacial bonding between feed-powder particles and the substrate in the cold-gas dynamic-spray process, Appl. Surf. Sci. 219 (2003) 211.
[22] S. Brossard, P.R. Munroe, A. Tran, M.M. Hyland, Study of the splat-substrate interface for a NiCr coating plasma sprayed onto polished aluminium and stainless steel substrates, J. Therm. Spray Tech. 19 (2010) 24.
[23] V.V. Sobolev, J.M. Guilemany, J. Nutting, J.R. Miquel, Development of substrate-coating adhesion in thermal spraying, Int. Mater. Rev. 42 (1997) 117.